

GaN/AlGa_N multiple quantum wells grown on transparent and conductive (-201)-oriented β -Ga₂O₃ substrate for UV vertical light emitting devices

I. A. Ajia,¹ Y. Yamashita,² K. Lorenz,³ M. M. Muhammed,¹ L. Spasevski,⁴ D. Almalawi,¹ J. Xu,¹ K. Iizuka,² Y. Morishima,² D. H. Anjum,⁵ N. Wei,⁵ R. W. Martin,⁴ A. Kuramata,² and I. S. Roqan^{1,a)}

¹King Abdullah University of Science and Technology (KAUST), Physical Sciences and Engineering Division, Thuwal, 23955, Saudi Arabia.

²Tamura Corporation and Novel Crystal Technology, Inc., Sayama, Saitama 350-1328, Japan.

³INESC-MN, IPFN, Instituto Superior Técnico, Campus Tecnológico e Nuclear, Bobadela LRS, Portugal.

⁴Department of Physics, SUPA, University of Strathclyde, Glasgow, G4 0NG, United Kingdom.

⁵King Abdullah University of Science and Technology (KAUST), Imaging and Characterization Core Laboratory, Thuwal, 23955, Saudi Arabia.

GaN/AlGa_N multiple quantum wells (MQWs) are grown on a ($\bar{2}01$)-oriented β -Ga₂O₃ substrate. The optical and structural characterizations of the MQW structure are compared with a similar structure grown on sapphire. Scanning transmission electron microscopy and atomic force microscopy images show that the MQW structure exhibits higher crystalline quality of well-defined quantum wells, when compared to a similar structure grown on sapphire. X-ray diffraction rocking curve and photoluminescence excitation analyses confirm a lower density of dislocation defects in the sample grown on β -Ga₂O₃ substrate. Detailed analysis of time-integrated and time-

^{a)} Author to whom correspondence should be addressed: iman.roqan@kaust.edu.sa

resolved photoluminescence measurements shows that the MQWs grown on the β -Ga₂O₃ substrate are of higher optical quality. Our work indicates that $(\bar{2}01)$ -oriented β -Ga₂O₃ substrate can be a potential candidate for UV vertical emitting devices.

III-nitride semiconductors are known for their mechanical durability, as well as wide and direct bandgap characteristics, making them ideal for many optoelectronics and photonics applications. However, their performance as light emitting devices is presently limited by excessive threading dislocation (TD) defects caused by lattice mismatch with suitably transparent substrates, such as Al_2O_3 (sapphire) with a lattice mismatch of $\sim 16\%$ with GaN.¹² One possible replacement candidate that has recently received significant attention is the transparent and conductive $(\bar{2}01)$ -oriented β - Ga_2O_3 substrate.³⁻⁶ Its main advantages stem from its lower effective mismatch with GaN ($\sim 4.7\%$),³ making it a promising candidate for mitigating the problem of high defect densities typically characterizing III-nitride materials grown on Al_2O_3 . Furthermore, β - Ga_2O_3 is a conductive oxide with characteristic transparency (down to 260 nm) in the UV region, which is highly beneficial for UV vertical light emitting diodes, including vertical cavity surface emitting lasers (VCSELs).^{5,7} This contrasts it sharply with other alternatives, such as conductive SiC that lacks UV transparency,⁸ and GaN that is not as transparent for deep UV as β - Ga_2O_3 (and is thus inadequate for AlGaIn growth) and is impossible to produce on large scale at reasonable costs.¹¹ Moreover, β - Ga_2O_3 is relatively cost-effective and easy to grow.^{9,10} GaN, InGaIn and AlGaIn layers have been previously grown on (100)-oriented β - Ga_2O_3 by metal organic chemical vapor deposition (MOCVD)^{12,13} and molecular beam epitaxy^{14,15} but the material quality was poor compared to that grown on Al_2O_3 . More recently, the quality of the GaN and AlGaIn epitaxial layers was slightly improved by employing facet controlled growth on β - Ga_2O_3 .¹⁶ However, the authors reported that, due to the strong cleavage nature of the (100) plane of β - Ga_2O_3 , the epilayer uncontrollably peeled off from the substrate, resulting in unstable devices. Therefore, $(\bar{2}01)$ -oriented β - Ga_2O_3 is well positioned as a suitable alternative substrate for use in vertical emitting devices, including those operating in the deep UV region. Recently, we reported on the growth of

a high-efficiency InGaN/GaN multiple quantum well (MQW) vertical LED on $(\bar{2}01)$ -oriented β -Ga₂O₃ substrate.¹⁷ However, UV emitting GaN/AlGaN MQW structure grown on $(\bar{2}01)$ -oriented β -Ga₂O₃ substrate has not yet been achieved.

In this work, we study the structural and optical properties of GaN/AlGaN MQW structures grown on $(\bar{2}01)$ -oriented β -Ga₂O₃ substrate. We compare their properties with MQWs grown on Al₂O₃. We demonstrate that $(\bar{2}01)$ -oriented β -Ga₂O₃ is a substrate with potential value for the growth of vertical UV emitting devices.

The MQW structure (Sample S1) was grown by MOCVD on $(\bar{2}01)$ -oriented β -Ga₂O₃. Trimethylgallium, trimethylaluminum and ammonia were used as precursors for epilayer growth. The growth commenced with a 2 nm low-temperature AlN buffer layer grown on $(\bar{2}01)$ -oriented β -Ga₂O₃ substrate at 550 °C. A 100 nm n-Al_{0.75}Ga_{0.25}N layer was then grown at 1020 °C, followed by a 900 nm thick n-Al_{0.30}Ga_{0.70}N layer at 1120 °C. The overgrown III-nitride epilayers crystalized with the *c*-plane (0001) parallel to the $(\bar{2}01)$ plane of the monoclinic β -Ga₂O₃, as shown elsewhere.³ N₂ and H₂ were used as the carrier gasses for the AlN buffer and the n-AlGa_{0.75}N layer, respectively. Subsequently, 3×Ga_{0.75}N MQW and 4×Al_{0.2}Ga_{0.8}N multiple quantum barriers (MQBs) with 3 nm and 10 nm nominal thicknesses, respectively, were overgrown on the AlGa_{0.75}N layer at 900 °C. The pressure inside the reactor was maintained at 100 mbar throughout the growth process. For comparison, a similar MQW structure (Sample S2) was grown on *c*-sapphire ((0001)-Al₂O₃) under the same conditions, with the exception of the AlN buffer layer, which was 8 nm thick for growth optimization.

High resolution X-ray diffraction (XRD) was performed on a Bruker AXS D8 Discover diffractometer using Cu K_{α1} radiation. A Göbel mirror and a 2-bounce Ge (2 2 0) monochromator were used in the primary beam and a 2-bounce Ge (2 2 0) analyzer was placed in front of a

scintillation detector in the secondary beam. Scanning transmission electron microscopy (STEM) was performed by Titan Themis Z 40–300 TEM. The surface morphology of the samples was examined by Agilent 5400 atomic force microscopy (AFM). Time-integrated photoluminescence (PL) was performed using a frequency-doubled Ar⁺ CW laser at 244 nm (an excitation power of 5 mW and a spot size of ~60 μm). The signal was detected by Andor SR-303i spectrograph and charge-coupled device (CCD) camera. The time-resolved photoluminescence (TRPL) was performed using frequency-tripled Ti:Sapphire pulsed laser (266 nm) with a pulse width of 150 fs and a pulse rate of 76 MHz. The Ti:Sapphire laser had an average excitation power of 3 mW and was focused to a diameter of ~60 μm, measured by a Gentec beam profiler. The signal was detected by an Acton spectrograph and Hamamatsu C5680 streak camera operating in a synchroscan mode with a temporal resolution of 2 ps. The samples were mounted in a closed-cycle He cryostat to vary the temperature between 6 K and room temperature (RT). Photoluminescence excitation (PLE) measurements were performed at RT using an Edinburgh Instrument FLS 980 fluorescence spectrometer attached to a 1000 W xenon arc lamp. Cathodoluminescence (CL) measurements were performed using the FEI Quanta 250 scanning electron microscope (SEM) with an electron voltage of 5 kV. SEM was coupled to a spectrograph and a CCD camera.

Fig. 1(a) shows the structural schematic of both samples. Fig. 1(b) provides the symmetric and asymmetric XRD rocking curve (RC) plots. The symmetric RC plots around the (004) reflection for the two samples are similar. However, the AlGa_N layer grown on Al₂O₃ (S2) shows a considerably broader peak for the (104) asymmetric reflection (measured in skew symmetry), suggesting a higher density of edge dislocations than that in the layer grown on (2̄01)-Ga₂O₃ (S1), as asymmetric reflection RCs are broadened by edge dislocations, whereas symmetric reflection RC peak broadening is sensitive to screw and mixed type dislocations.¹⁸

Fig. 1(c) shows the false color AFM topography of S1 and S2, both of which exhibit extensive surface defects. S1 is characterized by high densities of V-pit defects (Fig. *S1* in Supplementary Material) and pseudo-trench defects, which can result from the coalescence of adjacent V-pits.^{19,20} However, we cannot completely rule out the presence of actual trench defects in S2 as it is characterized by higher density of trench defects relative to S1. Due to their extensive overlap with V-pits, we are unable to quantify the density of V-pits and trench defects in S2. Nonetheless, the overall density of surface defects in S2 is significantly greater (about 1.3 times) than that observed in S1 (Fig. *S2* in Supplementary Material).

Fig. 1(d) shows the Z-contrast cross-section STEM images of the n-Al_{0.27}Ga_{0.73}N buffer layer for both structures, followed by a 1 nm Al-rich layer. This Al-rich layer was unintentionally grown and likely originates from the change in precursor conditions between the n-AlGaN layer and the first quantum barrier. When the precursor flow is interrupted during MOCVD growth, desorption of Ga atoms can occur due to the high temperature required for growth.²¹ Following this layer, well-defined GaN/AlGaN MQWs are observed. The average thicknesses of the MQWs and MQBs are 3.2 nm and 10.3 nm, respectively. We observe V-pits and trench defects, in both samples, emerging from the MQW/MQB layers. The V-pits preferentially emerge from screw and mixed type TDs.^{22,23} However, the trench defects, while resembling V-pits when observed by STEM,²⁴ were found to emerge from stacking mismatch boundaries that terminate the basal plane stacking faults.^{25,26} Both trench defects and V-pits act as strain relief mechanisms in highly strained layers.^{23,25} Thus, the higher concentration of both defect types in S2 may be due to the relatively higher stress experienced by the MQW/MQB layers compared to those comprising S1.³ STEM results also reveal that MQW degradation around the defects is more severe in S2 than in S1.

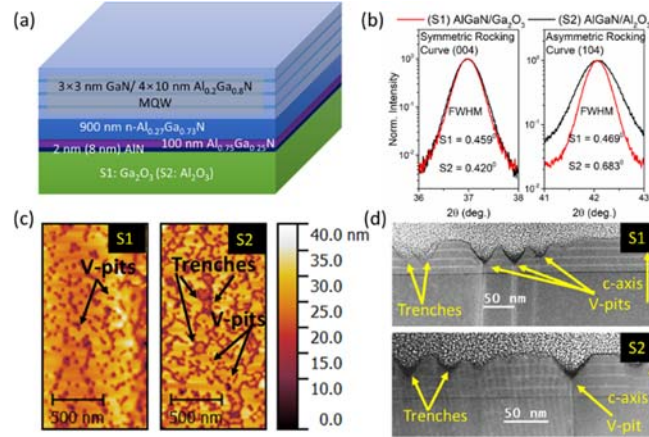


Fig. 1. (a) Structural schematic of the samples. (b) Symmetric (004) and skew symmetric (104) XRD RCs, (c) AFM images and (d) cross-sectional STEM images of the MQW structures of S1 (grown on $\bar{2}01$ -oriented Ga_2O_3) and S2 (grown on Al_2O_3).

Fig. 2(a) and 2(b) show the CW PL spectra of the near band edge emission (NBE) at 13 K. The MQW PL peaks due to donor-bound exciton (D^0X) recombination are located at 3.384 eV and 3.367 eV for S1 and S2, respectively, which represents a blueshift of 17 meV for the sample on $\beta\text{-Ga}_2\text{O}_3$. This blueshift may be related to strain relaxation²⁷ in structures grown on $\beta\text{-Ga}_2\text{O}_3$ substrates, as confirmed in extant studies.^{3,4} We observe secondary peaks centered at 3.81 eV and 4.10 eV in the spectra of both samples, belonging to the $\text{Al}_{0.2}\text{Ga}_{0.8}\text{N}$ MQBs and $\text{Al}_{0.27}\text{Ga}_{0.73}\text{N}$ layers, respectively. The shoulder peaks on the low energy side of the MQW peaks are signatures of longitudinal optical (LO) phonon replicas and donor-acceptor pairs.^{28,29} The MQW D^0X peaks have a full width at half maximum of 66 meV and 73 meV for S1 and S2, respectively, suggesting that the MQW sample grown on Ga_2O_3 has a better crystalline quality than that grown on Al_2O_3 .

The high energy shoulders of the MQW peaks in both structures can be related to well-barrier thinning or intermixing around the V-pits and trench defects, as confirmed by RT CL hyperspectral imaging shown in Fig. 3(a-d) (and Fig. S4 in Supplementary Material) as well as STEM images (Fig. S3 in Supplementary Material). The emission signature of V-pits is observed,

as shown in Fig. 3(a). We extracted the CL spectra inside (point A) and away from the V-pits (point B). For S1, we are able to clearly resolve a high energy peak at 3.52 eV, as well as the MQW peak at 3.38 eV, whereas we observe only the MQW peak at point B. For S2, the V-pits are less resolvable, as shown in the CL spectra (Fig. 3(b)). However, we identify regions with (point C) and without (point D) trench loop defects. The CL spectra show that there is no clear peak splitting inside the trench loop of S2 (Fig. 3(d)). However, we can still observe the signature of high energy shift around the trench defect, compared to the trench-free part (point D).

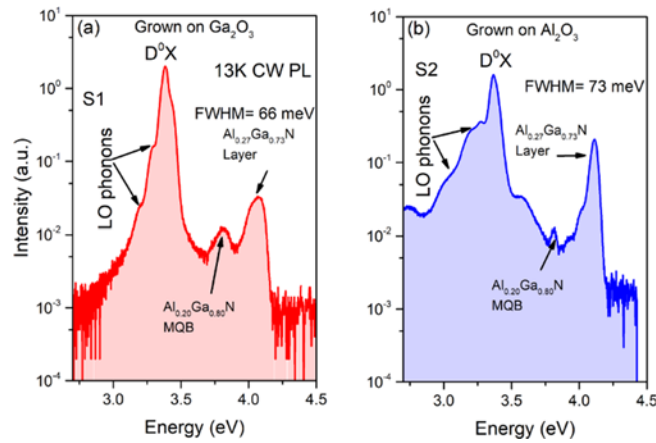


Fig. 2. Low temperature (13 K) PL spectra of the NBE emissions of (a) S1 and (b) S2.

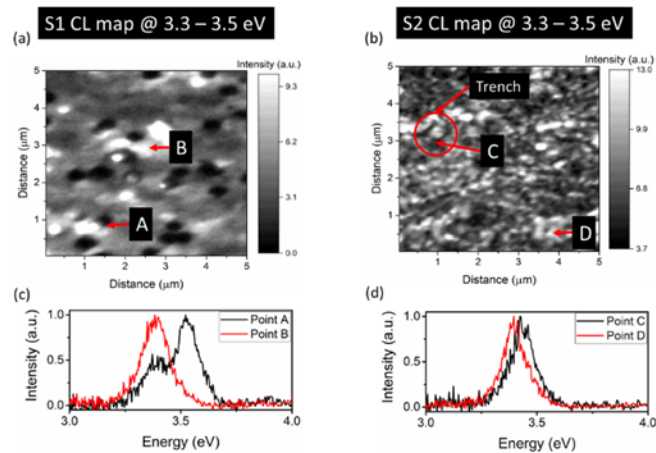


Fig 3. (a, b) CL hyperspectral intensity maps of S1 and S2, respectively; (c, d) CL spectra for selected points A and B taken from S1 and points C and D taken from S2 CL maps, respectively.

To investigate the carrier dynamics, temperature-dependent PL and TRPL were studied. Fig. 4(a) shows the temperature dependence of the PL NBE energy using pulsed laser excitation, as it has a much higher laser power density compared to our CW laser, and can reveal the NBE peak at higher temperatures. Both samples exhibit the known s-shape dependence of NBE energy on temperature typical of exciton localization in III-nitride MQW structures.³⁰⁻³² There is an initial redshift in the energy peak as temperature increases from 5 K to ~60 K, indicating carrier relocation to lower energy states. Subsequently, a blueshift commences within the 60–110 K temperature range. In this range, as the carriers are delocalized due to thermal activation, they are more easily trapped by non-radiative recombination sites. Beyond 110 K, the peak energies of both samples redshift monotonously, as predicted by Varshni.³³ Furthermore, at 15 K, the NBE peaks of both samples (3.44 eV and 3.42 eV for S1 and S2, respectively) are shifted slightly to higher energies compared to the values obtained by CW excitation. The disparity in the results is due to higher ($\sim 10^9$ times) excitation power of the pulsed laser. Thus, such blueshift occurs by first Coulomb screening of quantum-confined Stark effect (QCSE) in the MQWs, followed by the filling of high energy band-tail states when defect states are sufficiently saturated.^{34,35}

Fig. 4(b) shows the pulsed excitation PL spectra for both samples at 15 K. The NBE integrated intensity of S1 is found to be ~ 10 times higher than that of S2 at the same excitation power and temperature. This 10-fold increase in the integrated intensity is confirmed by PL measurements using RT CW excitation, as shown in the inset of Fig. 3(b), whereas the yellow luminescence (YL) band intensity is lower in S1.

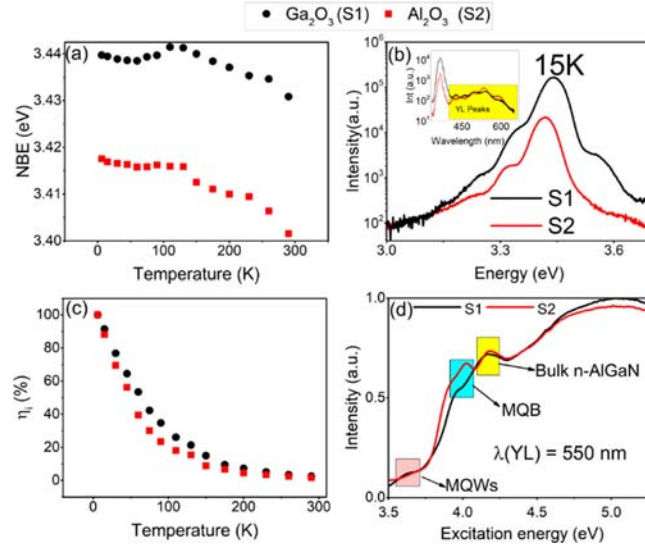


Fig. 4. (a) Temperature dependence of NBE energy, (b) PL spectra at RT. (Inset: CW excitation spectra at RT), (c) temperature dependence of IQE, and (d) PLE spectra at 550 nm of S1 and S2.

We perform PLE measurements to gain insight into the possible cause of the S1 peak intensity increase. Fig. 4(d) shows the PLE spectra at 550 nm. The two samples have nearly identical YL dominated by deep level defects (DLDs) in the bulk n-AlGaN layer, located at 4.2 eV (yellow shaded region). However, the YL related to the DLDs in the MQBs (blue-shaded region, 4 eV) behaves differently. The YL of the MQBs of S2 is more prominent than that of S1. This difference implies a higher density of defects in the MQB/MQW region of S2 compared to S1. It has been shown that point defects, widely believed to be responsible for the YL peak in III-nitrides, preferentially form around edge type TDs.³⁶ This result is consistent with the RC findings. In the light-red shaded region around 3.6 eV, which corresponds to the YL contribution from the MQWs, the peaks are similar. However, the band edge of the MQWs of S2 is not well defined, possibly due to the combined prominence of trench loops and V-pit defects in S2, compared to S1, as confirmed by AFM.

We compared their relative internal quantum efficiency (IQE), $\eta_i(T)$, as the ratio of the PL integrated intensity (in the 3.2–3.65 eV range) at each temperature relative to that at the lowest

temperature (5 K) by assuming that the non-radiative channels are inactive at 5 K (in line with the approach used in Rashba's treatment).³⁷⁻³⁹ The IQE of S1 is found slightly higher than that of S2 in the measured temperature range. At RT, S1 had an IQE of 2.6%, whereas S2 had an IQE of 1.8%. This slight improvement in the IQE of S1 can be attributed to the lower density of edge type dislocations, as shown in the RC results (Fig. 1(b)).

We carried out temperature-dependent TRPL measurements to further understand the carrier dynamics of both samples. Fig. 5(a) and 5(b) show the TRPL spectra at 6 K and RT of S1 and S2, respectively. The PL decay curves of both samples are non-exponential at all temperatures. The carrier lifetime was calculated using the method shown in *Sec. 4* of Supplementary Material. The model (solid lines in Fig. 5(a) and 5(b)) provides excellent fit to the experimental data. For the purpose of our analyses, we used the slow decay lifetimes as the steady state PL lifetimes, to avoid the complications caused by other fast phenomena, such as hot carrier-phonon interactions and decay of optical phonons, which occur within the 1–100 ps range.⁴⁰ The total TRPL (τ_{TRPL}) lifetimes for S1 are 1.13 ns (6 K) and 0.62 ns (RT), whereas 0.66 ns (6 K) and 0.37 ns (RT) are measured for S2.

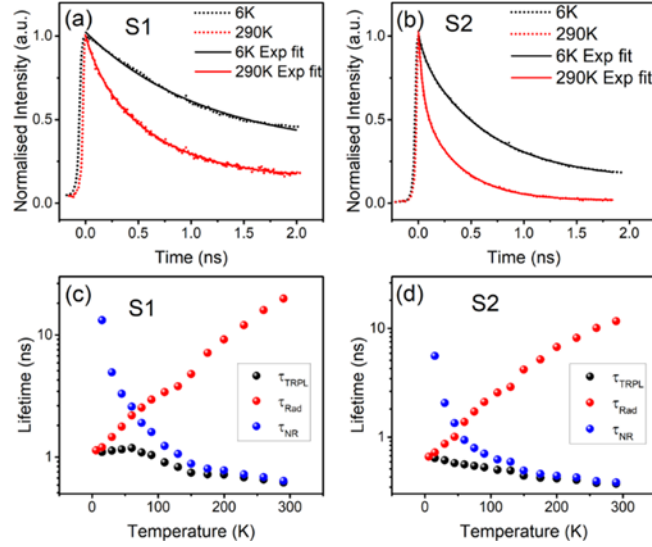


Fig. 5. RT and 6 K TRPL spectra of MQW structures of (a) S1 and (b) S2. Temperature-dependent lifetime parameters for (c) S1 and (d) S2.

By assuming that the radiative recombination in each sample reaches maximum at low temperature, radiative, τ_{rad} , and non-radiative, τ_{nr} recombination lifetimes are extracted.⁴¹ Fig. 5(c) and 5(d) show the temperature dependence of τ_{TRPL} , τ_{rad} and τ_{nr} for S1 and S2, respectively. Both samples exhibit a monotonous increase in radiative recombination across the entire temperature range, while the non-radiative recombination rapidly decreases with increasing temperature. In both samples, non-radiative phenomena become the dominant carrier recombination mechanism at ~ 60 K, which coincides with the temperature at which the carrier delocalization process is observed in the temperature-dependent PL in Fig. 4(a). Both the radiative carrier lifetime— $\tau_{rad} = 1.13$ ns (6 K) and 19.78 ns (RT) — and the non-radiative carrier lifetime— $\tau_{nr} = 0.64$ ns (RT) — of S1 are observed to be about twice as long as those of S2— $\tau_{rad} = 0.66$ (6 K) and 11.66 ns (RT), whereas $\tau_{nr} = 0.38$ ns (RT). The longer τ_{nr} measured for S1 is attributed to the lesser contribution from non-radiative effect in the recombination process,⁴²⁻⁴⁴ as a result of the lower density of defects in S1 (consistent with our PLE and RC results). However, S1 has longer τ_{rad} relative to S2, which could be attributed to a less pronounced electron-hole wavefunction overlap resulting from

the strain relaxation. As was previously discussed, the III-nitride layers overgrown on $(\bar{2}01)$ -oriented Ga_2O_3 (S1) have been shown to be more strain relaxed than those grown on Al_2O_3 . While this can lead to low rates of radiative recombination processes (longer τ_{rad}),⁴⁵ the decline in overlap probability can effectively be offset by the higher crystalline quality of the overgrown layer, leading to better optical performance.⁴⁶

In conclusion, GaN/AlGaN MQWs were grown on $(\bar{2}01)$ -oriented $\beta\text{-Ga}_2\text{O}_3$ substrate. Structural and optical analyses revealed that, in the absence of enhanced growth techniques, a generally higher structural and optical quality of MQW growth was achieved on $(\bar{2}01)$ -oriented $\beta\text{-Ga}_2\text{O}_3$ when compared to a similar structure grown on Al_2O_3 substrate. Carrier lifetime analyses confirmed that the density of non-radiative recombination centers in MQWs grown on $(\bar{2}01)$ -oriented $\beta\text{-Ga}_2\text{O}_3$ was lower compared to that in MQWs grown on Al_2O_3 . Thus, under systematically optimized conditions, growth of highly efficient vertical UV emitting devices based on III-nitrides (including VCSELs) on $\beta\text{-Ga}_2\text{O}_3$ substrates should be possible, allowing for device designs that would benefit from the transparent and conductive properties of $\beta\text{-Ga}_2\text{O}_3$.

Supplementary material

See supplementary material for defect density estimation methods, STEM and CL images confirming well/barrier thinning and intermixing as well as the method employed when calculating carrier lifetimes.

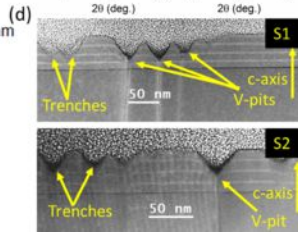
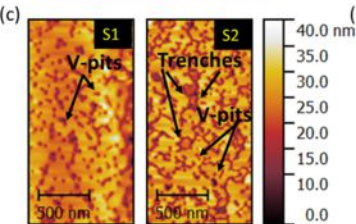
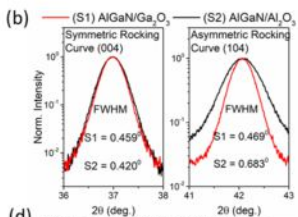
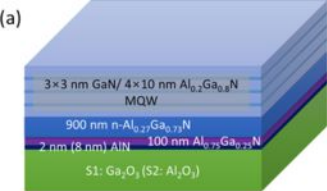
Acknowledgements

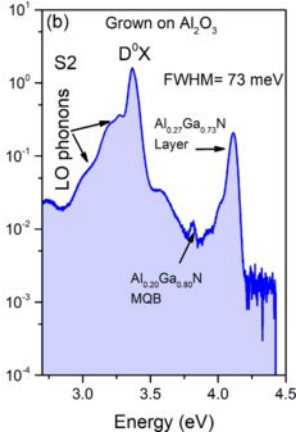
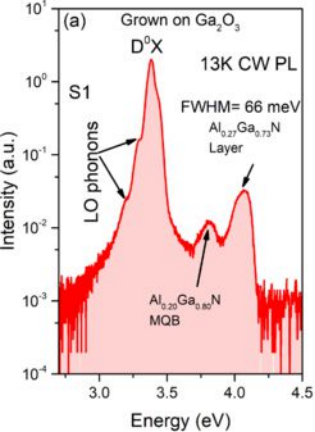
The authors thank KAUST for financial support.

References

- 1 S. D. Lester, F. A. Ponce, M. G. Craford, and D. A. Steigerwald, *Appl. Phys. Lett.* **66**, 1249 (1995).
- 2 S. A. Kukushkin, A. V. Osipov, V. N. Bessolov, B. K. Medvedev, V. K. Nevolin, and K. A. Tcarik, *Rev. adv. mater. sci.* **17**, 1 (2008).
- 3 M. M. Muhammed, M. Peres, Y. Yamashita, Y. Morishima, S. Sato, N. Franco, K. Lorenz, A. Kuramata, and I. S. Roqan, *Appl. Phys. Lett.* **105**, 042112 (2014).
- 4 M. M. Muhammed, M. A. Roldan, Y. Yamashita, S. L. Sahonta, I. A. Ajia, K. Iizuka, A. Kuramata, C. J. Humphreys, and I. S. Roqan, *Sci. Rep.* **6**, 29747 (2016).
- 5 Z. Hajnal, J. Miró, G. Kiss, F. Réti, P. Deák, R. C. Herndon, and J. M. Kuperberg, *J. Appl. Phys.* **86**, 3792 (1999).
- 6 H. Murakami, K. Nomura, K. Goto, K. Sasaki, K. Kawara, Q. T. Thieu, R. Togashi, Y. Kumagai, M. Higashiwaki, A. Kuramata, S. Yamakoshi, B. Monemar, and A. Koukitu, *Appl. Phys. Express* **8**, 015503 (2015).
- 7 W. Mi, X. Du, C. Luan, H. Xiao, and J. Ma, *RSC Adv.* **4**, 30579 (2014).
- 8 S. Kim, J. E. Spanier, and I. P. Herman, *Jpn. J. Appl. Phys.* **39**, 5875 (2000).
- 9 V. N. Maslov, V. M. Krymov, M. N. Blashenkov, A. A. Golovatenko, and V. I. Nikolaev, *Tech. Phys. Lett.* **40**, 303 (2014).
- 10 J. Zhang, C. Xia, Q. Deng, W. Xu, H. Shi, F. Wu, and J. Xu, *J. Phys. Chem. Solids* **67**, 1656 (2006).
- 11 K. Gurnett and T. Adams, *III-Vs Review* **19**, 39 (2006).
- 12 H. Aida, K. Nishiguchi, H. Takeda, N. Aota, K. Sunakawa, and Y. Yaguchi, *Jpn. J. Appl. Phys.* **47** (11R), 8506 (2008).
- 13 K. Shimamura, E. G. Villora, K. Domen, K. Yui, K. Aoki, and N. Ichinose, *Jpn. J. Appl. Phys.* **44**, L7 (2005).
- 14 E. G. Villora, S. Arjoca, K. Shimamura, D. Inomata, and K. Aoki, *Proc. SPIE* **8987**, Oxide-based Materials and Devices V, 89871U (2014).
- 15 E. G. Villora, K. Shimamura, K. Kitamura, K. Aoki, and T. Ujiie, *Appl. Phys. Lett.* **90**, 234102 (2007).
- 16 S. Ito, K. Takeda, K. Nagata, H. Aoshima, K. Takehara, M. Iwaya, T. Takeuchi, S. Kamiyama, I. Akasaki, and H. Amano, *Phys. Stat. Sol. (c)* **9**, 519 (2012).
- 17 M. M. Muhammed, N. Alwadai, S. Lopatin, A. Kuramata, and I. S. Roqan, *ACS. Appl. Mater. Inter.* **9**, 34057 (2017).
- 18 Y. J. Sun, O. Brandt, T. Y. Liu, A. Trampert, K. H. Ploog, J. Blasing, and A. Krost, *Appl. Phys. Lett.* **81**, 4928 (2002).
- 19 J. Bruckbauer, P. R. Edwards, T. Wang, and R. W. Martin, *Appl. Phys. Lett.* **98**, 141908 (2011).
- 20 F. C.-P. Massabuau, S.-L. Sahonta, L. Trinh-Xuan, S. Rhode, T. J. Puchtler, M. J. Kappers, C. J. Humphreys, and R. A. Oliver, *Appl. Phys. Lett.* **101**, 212107 (2012).
- 21 X. Li, S. Sundaram, P. Disseix, G. Le Gac, S. Bouchoule, G. Patriarche, F. Réveret, J. Leymarie, Y. El Gmili, T. Moudakir, F. Genty, J. P. Salvestrini, R. D. Dupuis, P. L. Voss, and A. Ougazzaden, *Opt. Mater. Express* **5**, 380 (2015).
- 22 I.-H. Kim, H.-S. Park, Y.-J. Park, and T. Kim, *Appl. Phys. Lett.* **73**, 1634 (1998).
- 23 K. S. Son, D. G. Kim, H. K. Cho, K. Lee, S. Kim, and K. Park, *J. Cryst. Growth* **261**, 50 (2004).

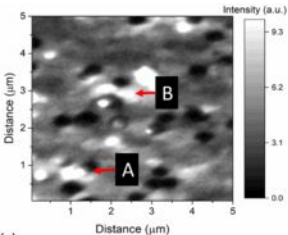
- 24 J. Bruckbauer, P. R. Edwards, S.-L. Sahonta, F. C. P. Massabuau, M. J. Kappers, C. J.
Humphreys, R. A. Oliver, and R. W. Martin, *J. Phys. D: Appl. Phys.* **47**, 135107 (2014).
- 25 J. Smalc-Koziorowska, E. Grzanka, R. Czernecki, D. Schiavon, and M. Leszczyński, *Appl.*
Phys. Lett. **106**, 101905 (2015).
- 26 F. C. P. Massabuau, C. C. Tartan, R. Traynier, W. E. Blenkhorn, M. J. Kappers, P. Dawson,
C. J. Humphreys, and R. A. Oliver, *J. Cryst. Growth* **386**, 88 (2014).
- 27 J. H. Son and J. L. Lee, *Opt. Express* **18**, 5466 (2010).
- 28 M. A. Reshchikov and H. Morkoç, *J. Appl. Phys.* **97**, 061301 (2005).
- 29 A. Ben Slimane, A. Najar, R. Elafandy, D. P. San-Román-Alerigi, D. Anjum, T. K. Ng,
and B. S. Ooi, *Nanoscale Res. Lett.* **8**, 342 (2013).
- 30 A. Yasan, R. McClintock, K. Mayes, D. H. Kim, P. Kung, and M. Razeghi, *Appl. Phys.*
Lett. **83**, 4083 (2003).
- 31 K. B. Lee, P. J. Parbrook, T. Wang, F. Ranalli, T. Martin, R. S. Balmer, and D. J. Wallis,
J. Appl. Phys. **101**, 053513 (2007).
- 32 I. A. Ajia, P. R. Edwards, Z. Liu, J. C. Yan, R. W. Martin, and I. S. Roqan, *Appl. Phys.*
Lett. **105**, 122111 (2014).
- 33 Y. P. Varshni, *Physica* **34**, 149 (1967).
- 34 J. Zhang and N. Tansu, *J. Appl. Phys.* **110**, 113110 (2011).
- 35 H. Wang, Z. Ji, S. Qu, G. Wang, Y. Jiang, B. Liu, X. Xu, and H. Mino, *Opt. Express* **20**,
3932 (2012).
- 36 J. Elsner, R. Jones, M. I. Heggie, P. K. Sitch, M. Haugk, Th Frauenheim, S. Öberg, and P.
R. Briddon, *Phys. Rev. B* **58**, 12571 (1998).
- 37 D. Iida, A. Fadil, Y. Chen, Y. Ou, O. Kopylov, M. Iwaya, T. Takeuchi, S. Kamiyama, I.
Akasaki, and H. Ou, *AIP Adv.* **5**, 097169 (2015).
- 38 T. Kohno, Y. Sudo, M. Yamauchi, K. Mitsui, H. Kudo, H. Okagawa, and Y. Yamada, *Jpn.*
J. Appl. Phys. **51** (7R), 072102 (2012).
- 39 O. Brandt, J. Ringling, K. H. Ploog, H. J. Wunsche, and F. Henneberger, *Phys. Rev. B* **58**,
15977 (1998).
- 40 J. Shah and Lucent Technologies (Firm), *Ultrafast spectroscopy of semiconductors and*
semiconductor nanostructures, 2nd enl. ed. (Springer Verlag, Berlin; New York, 1999),
pp.xvi.
- 41 T. Li, A. M. Fischer, Q. Y. Wei, F. A. Ponce, T. Detchprohm, and C. Wetzel, *Appl. Phys.*
Lett. **96**, 031906 (2010).
- 42 J. Dekker, A. Tukiainen, N. Xiang, S. Orsila, M. Saarinen, M. Toivonen, M. Pessa, N.
Tkachenko, and H. Lemmetyinen, *J. Appl. Phys.* **86**, 3709 (1999).
- 43 V. Liuolia, A. Pinos, S. Marcinkevičius, Y. D. Lin, H. Ohta, S. P. DenBaars, and S.
Nakamura, *Appl. Phys. Lett.* **97**, 151106 (2010).
- 44 Y. Li, D. P. Byrnes, and E. B. Stokes, *ECS J. Solid State Sci. Technol.* **2**, R267 (2013).
- 45 C. Du, X. Huang, C. Jiang, X. Pu, Z. Zhao, L. Jing, W. Hu, and Z. L. Wang, *Sci. Rep.* **6**,
37132 (2016).
- 46 S. A. Al Mueeed, W. Sun, X. L. Wei, R. B. Song, D. D. Koleske, N. Tansu, and J. J. Wierer,
AIP Adv. **7** (10), 105312 (2017).



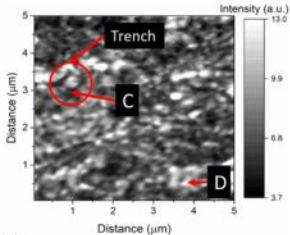


S1 CL map @ 3.3 – 3.5 eV

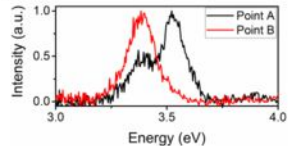
(a)

**S2 CL map @ 3.3 – 3.5 eV**

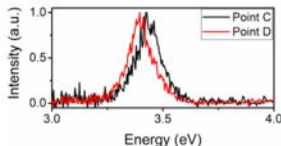
(b)



(c)



(d)



● Ga₂O₃ (S1) ■ Al₂O₃ (S2)

